Neutral tropical African CO_2 exchange estimated from aircraft and satellite observations

[1]Benjamin Gaubert, [2]Britton B. Stephens, [3]David F. Baker, [4,5]Sourish Basu, [6]Michael Bertolacci [7]Kevin W. Bowman, [1]Rebecca Buchholz, [7]Abhishek Chatterjee, [8]Frédéric Chevallier, [9]Róisín Commane, [6]Noel Cressie, [10]Feng Deng, [3]Nicole Jacobs, [11]Matthew S. Johnson, [12]Shamil S. Maksyutov, [13,14]Kathryn McKain, [7]Junjie Liu, [15]Zhiqiang Liu, [16]Eric Morgan, [3]Chris O'Dell, [17]Sajeev Philip, [18]Eric Ray, [7]David Schimel, [3]Andrew Schuh, [3]Thomas E. Taylor, [19,20]Brad Weir, [21]Dave van Wees, [22]Steven C. Wofsy, [6]Andrew Zammit-Mangion [23]Ning Zeng

[1]Atmospheric Chemistry Observations & Modeling Laboratory (ACOM), National Center for Atmospheric Research, Boulder, CO, 80301

[2]Earth Observing Laboratory (EOL), National Center for Atmospheric Research, Boulder, CO, 80301

[3]cooperative Institute for Research in the Atmosphere, Colorado State University, Fort Collins, CO, USA

[4]Global Modeling and Assimilation Office, National Aeronautics and Space Administration, Goddard Space Flight Center, Greenbelt, MD 20771.

[5]Earth System Science Interdisciplinary Center, University of Maryland, College Park, MD 20740.

[6]School of Mathematics and Applied Statistics, University of Wollongong, Wollongong, Australia

[7]Jet Propulsion Laboratory, California Institute of Technology, Pasadena, CA, USA

[8]Laboratoire des Sciences du Climat et de L'Environnement, Institut Pierre-Simon Laplace, CEA-CNRS-UVSQ, Gif sur Yvette, 91191 CEDEX, France

[9]Dept of Earth & Environmental Sciences, Lamont-Doherty Earth Observatory, Columbia University, Palisades, NY 10964

[10]Department of Physics, University of Toronto, Toronto, Ontario, Canada

[11]Earth Science Division, NASA Ames Research Center, Moffett Field, CA, USA

[12]National Institute for Environmental Studies, Tsukuba, Japan

[13]Cooperative Institute for Research in Environmental Sciences, University of Colorado Boulder, Boulder, CO, 80309

[14]NOAA Global Monitoring Laboratory, Boulder, CO, 80309

[15]State Key Laboratory of Numerical Modeling for Atmospheric Sciences and Geophysical Fluid Dynamics, Institute of Atmospheric Physics, Chinese Academy of Sciences, Beijing, China

[16]Scripps Institution of Oceanography, University of California, San Diego, USA 92037

[17]Centre for Atmospheric Sciences, Indian Institute of Technology Delhi, New Delhi 110 016, India

[18]NOAA Chemical Sciences Laboratory, Boulder, CO, 80309

[19]Universities Space Research Association, Columbia, MD, USA

[20]NASA Goddard Space Flight Center, Greenbelt, MD, USA

[21]Faculty of Science, Vrije Universiteit, 1081HV Amsterdam, The Netherlands

[22]School of Engineering and Applied Science and Department of Earth and Planetary Sciences, Harvard University, Cambridge, MA, USA

[23]Dept. of Atmospheric and Oceanic Science and Earth System Science Interdisciplinary Center, University of Maryland, College Park, MD, USA

1. OCO-2 filtering and bias correction

The v10 MIP assimilates OCO-2 retrievals produced by the Atmospheric Carbon Observations from Space (ACOS) B10 (O'Dell et al., 2012; Kiel et al., 2019) algorithm. The algorithm retrieves column average dry-air mole fraction of CO_2 in the atmosphere (XCO2) using solar reflectance spectra centered around 1.6 and 2.0 μm for CO_2 and 0.76 μm for O_2 to estimate the air mass. The retrievals optimize a state vector of 60 elements with nine parameters related to clouds and aerosols, including retrieved aerosol optical depth (AOD). The post-retrieval data processing also includes a quality filtering and a bias correction procedure. The filtering of bad quality data is made by applying a series

of threshold-based filters (Kiel et al., 2019). Figure S1b shows the fraction of Dec–Mar data that passed all the quality filter tests. Figure S1d,f shows retrieved AOD by OCO-2 for Dec–Mar, before and after quality filtering, respectively.

The parametric bias correction is derived from a multivariate regression between XCO2 spurious variability and parameters in the retrieval state vector. The bias correction over western NTA during Dec–Mar is 2.7 ppm on average (Figure S1a). Errors in retrieved surface pressure with respect to reanalyses, the dP term, contribute about 1 ppm over west Africa (Figure S1c) while the dust, water cloud, and sea salt (DWS) aerosol term adds slightly less than a 1 ppm (Figure S1e). The bias correction is defined globally, and NTA lacks in situ validation data. One possible explanation for the positive flux biases in LNLG inversions might be that this correction is too large in the version 10 OCO-2 product, and has also been too large in earlier version. We looked at the relationship between NTA fluxes estimated during the dry season and posterior XCO2 simulated by the v10 MIP. We subtracted XCO2 averaged for the entire globe except for over NTA from that averaged over NTA for each inversion to isolate at NTA anomalies, as the inversions differ widely on global average posterior XCO2. We find a linear relationship with higher posterior XCO2 resulting from higher fluxes, and the LNLG experiment having the highest XCO2 and fluxes during these 4 months (DJFM, Fig. S2). The linear regression of the individual model points has an r^2 of 0.56 and a slope of 4.16 PgC yr^{-1} per ppm. This slope implies that a flux error of 1 PgC yr$^-$1 could result from an XCO2 bias of +0.75 ppm if entirely within DJFM, or +0.25 ppm if the bias persisted all year. We calculated the same NTA XCO2 anomaly from the observations, both before and after the bias correction, and show these as vertical lines in Fig. S2. The bias correction leads to an increase of 0.73 ppm for the NTA XCO2 anomaly.

2. Fire emission estimates

We compare three different bottom-up fire emission estimates that are available for the African continent in 2016, FireCCISFD11, MCD64A1 (Ramo et al., 2021), and GFED4s (van der Werf et al., 2017). We show burned area and monthly emissions for the NTA region only (Fig. S3). The Global Fire Emissions Database with small fires (GFED4s) uses the 500 m MODIS MCD64A1 Collection 5.1 (C5.1) burned area product and additional small-fire burned areas derived using active fire detections. Burned area is combined with fuel load and fuel consumption estimates based on the Carnegie–Ames–Stanford Approach (CASA) biogeochemical model to estimate emissions at 0.25°x0.25° (van der Werf et al., 2017). van Wees and van der Werf (2019) adapted the GFED modelling framework to calculate emissions at 500 m, and used MCD64A1 C6 burned area. The FireCCISFD11 and MCD64A1 emission estimates are both based on the 500-m fire emission model (van Wees & van der Werf, 2019), where the MCD64A1 estimate is based on MODIS MCD64A1 500-m burned area and the FireCCISFD11 estimate is based on the Sentinel-2 20-m burned area product, which detects 80 % more burned area than MCD64A1. While the MCD64A1 C6 product includes more burned area than C5.1, GFED4s still includes more burned area because of the small fire algorithm (Fig. S3A).

The combination of lower burned area and the higher resolution of the 500 m model led to a net reduction in emissions compared to GFED4s, as illustrated for NTA in Figure S3B. The annual total NTA emissions for 2016 went from 0.46 PgC for GFED4s to 0.29 PgC for the 500 m model. The third estimate (Ramo et al., 2021) also employed a 500 m model (van Wees & van der Werf, 2019), but used higher-resolution 20 m burned area observations from the Sentinel-2 FireCCISFD11 instead of MCD64A1 C6. As a result of substantially more detected burned area at 20 m resolution (63 % more burned area than GFED4s), Sentinel-2 FireCCISFD11 estimates a larger annual total for 2016 of 0.55

PgC, and notably higher emissions during Mar-May at the end of the dry season when the other two estimates are much lower. We also show two fire emission estimates constrained by CO observations from the Measurements of Pollution in the Troposphere (MOPITT) with two different inversion system, the CMS-Flux-4DVAR (Bowman et al., 2017) and the CMS-Flux-LETKF (Miyazaki et al., 2020). The CO-based emission estimates are based upon a 4°x5° grid and so have a slightly coarser representation. The CO-based approaches are between the other estimates with substantial differences in March 2016. For NTA, the annual mean fire emissions for 2016 are 0.46 PgC yr^{-1} (GFED4s), 0.29 PgC yr^{-1} (MCD64A1), and 0.55 PgC yr^{-1} for FireCCISFD11. For the CO-based estimates, despite their different seasonality, their annual mean fire emissions remain close to the GFED4s with 0.45 PgC yr^{-1} for the CMS-Flux-LETKF and 0.43 PgC yr^{-1} the CMS-Flux-4DVAR.

During ATom-4, the ATom-EC indicates a dry-to-wet transition season flux of -0.26 ± 0.37 PgC yr^{-1} (mean±standard-deviation), while all the inversions suggest small positive fluxes. Fig. 3 shows large concentrations of HCN below the optimized ATom-4 subregion, indicating a biomass burning signature. Small agricultural fires are set to burn crop waste, and to clear the land for the next planting season (Yevich & Logan, 2003; Curtis et al., 2018; Hickman et al., 2021). This practice could explain the presence of small fires detected at higher spatial resolution including for the month of April and May in NTA. This is illustrated on Fig. S3 where the FireCCISFD11 estimate shows larger emissions than GFED4s for the months of March, April and May 2016. It is possible that despite finding a stronger correlation with all NTA fluxes, the optimized ATom-4 region undersamples fire influence (see next section). However, comparing back-trajectory footprints (Fig. S5) and CO concentrations (Fig. 4) shows reasonably good spatial correspondence.

3. Sensitivity to the choice of box boundaries

We quantify the impact of the choice of alternate box boundaries on our flux estimates via the flux-ΔCO_2 emergent constraint relationships. Fig. S4 shows the location of the top 12 highest correlation derived boxes for each campaign. These are all in similar locations generally with shifts by 5 degrees and 100 hPa around the optimal box, with the exception of ATom-4 which shows alternate boxes capturing the fire plume mentioned above. In these lower boxes, the CO_2 concentrations are higher and the ATom-4 emergent constraint produces positive flux estimates averaging between 0 and 2 PgC yr^{-}1 in closer agreement with the inversions. For each ATom we use these 12 different boxes to calculate monthly fluxes and the 10^4 combinations of these to calculate annual mean fluxes. The mean of all the annual estimates is 0.28 PgC yr^{-1} (similar to our optimal estimate of 0.14 PgC yr^{-1}) with a standard deviation of 0.1 PgC yr^{-1}. We add this standard deviation in quadrature with other components of our uncertainty estimate (see Materials and Methods).

4. Back trajectories

The global 14-day land flux contributions are shown in Fig. S5 for NTA-optimized boxes.

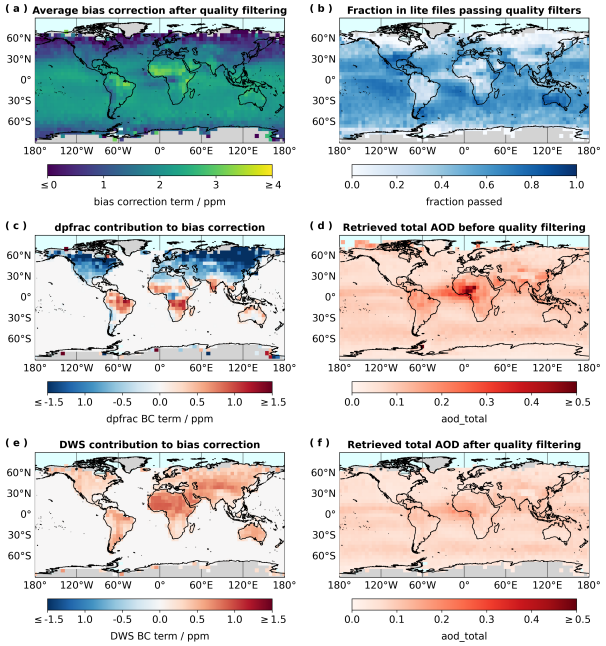

Figure S1. Aspects of the OCO-2 B10 Dec-Mar filtering and bias correction. A) Average bias correction after quality filtering. B) Fraction of observations passing quality filters. C) Bias correction caused by the dpfrac term. D) OCO-2 retrieved AOD before quality filtering. E) bias correction due to the dust, water cloud, and sea salt (DWS). F) OCO-2 retrieved AOD after quality filtering. All plots present December through March (2014-2019) averages and are aggregated into 5° × 5° latitude–longitude square bins.

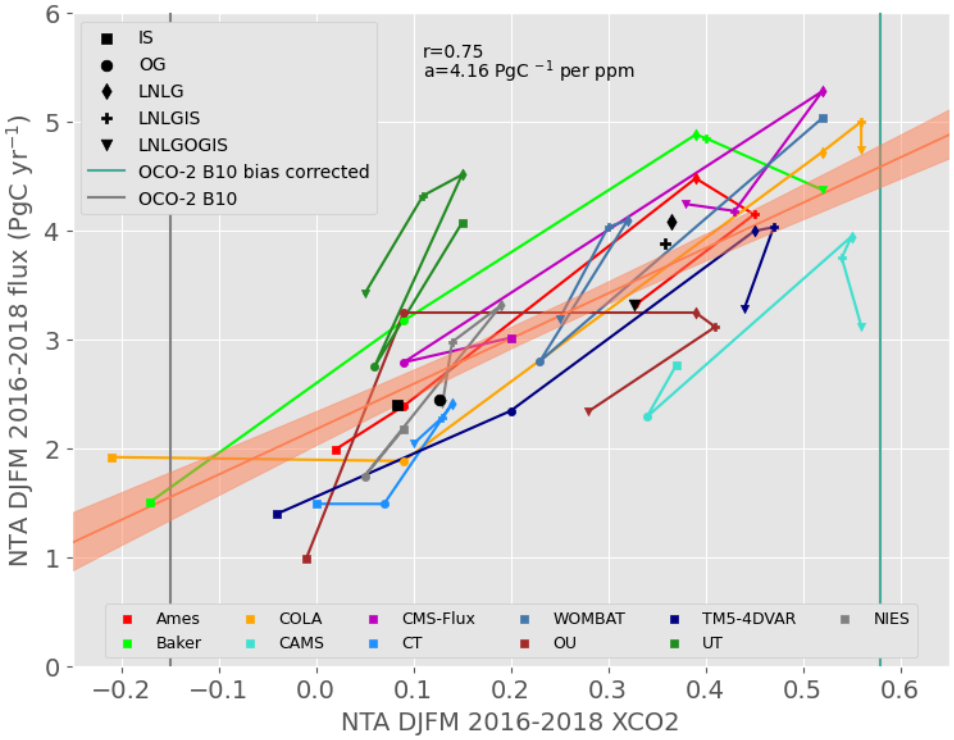

Figure S2. Dec-Mar mean net land CO_2 fluxes averaged over NTA (2016-2018) versus XCO2 simulated by the v10 MIP for NTA relative to the rest of the world. Black symbols show experiment means. The same NTA XCO2 anomaly metric for the observations is shown as vertical lines for with and without the bias correction.

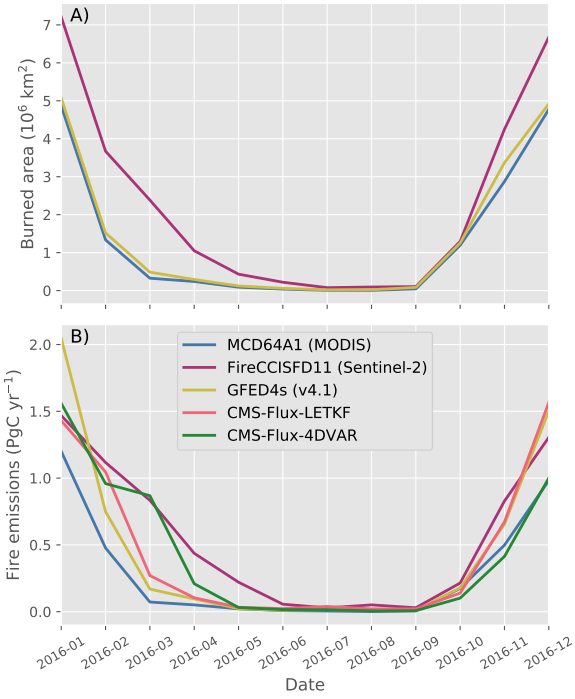

Figure S3. A) 2016 NTA monthly burned area and B) mean fire emissions estimated by MCD64A1, FireCCISFD11, GFED4s, CMS-Flux-4DVAR (Bowman et al., 2017) and CMS-Flux-LETKF (Miyazaki et al., 2020).

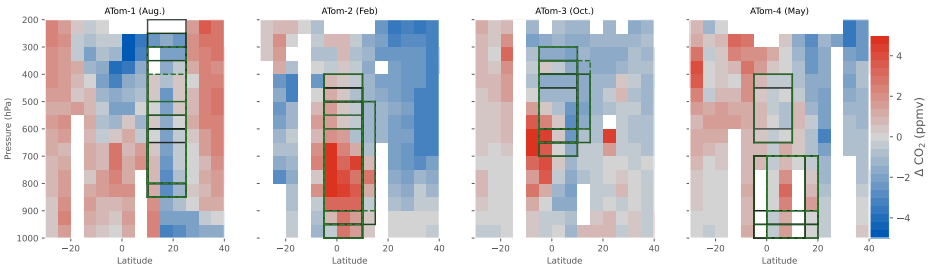

Figure S4. The top 12 highest correlation boxes for each campaign. Color shading shows the distribution of observed ΔCO_2 as in Fig. 1. The highest 5 (rank 1-5) are delineated by dark dashed lines, the second 7 (rank 5-12) by green solid lines. Lighter pinks represents smaller correlations. Bins containing no flight data are white. Note that all 12 boxes are different despite the apparent redundancy due to inclusion of bins with no data.

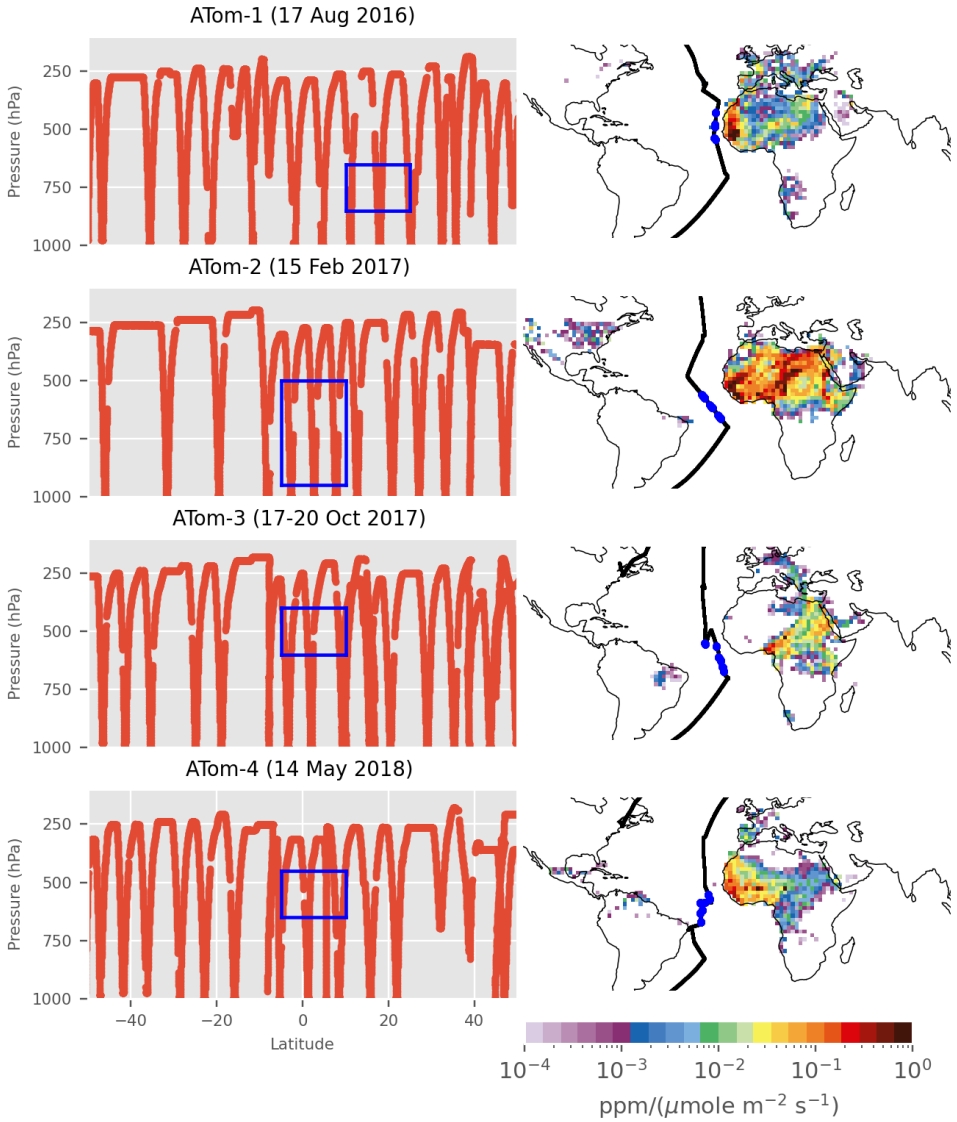

Figure S5. Left column: Pressure-latitude coverage of the NOAA Picarro CO_2 measurements from the ATom DC-8 flights in the Atlantic basin. Optimized boxes for NTA influence are shown in blue and dates intersecting these boxes are listed above each panel. Right column: 14-day footprints averaged over the NTA optimized boxes. The locations of the measurements made within the optimized boxes are indicated by blue dots.

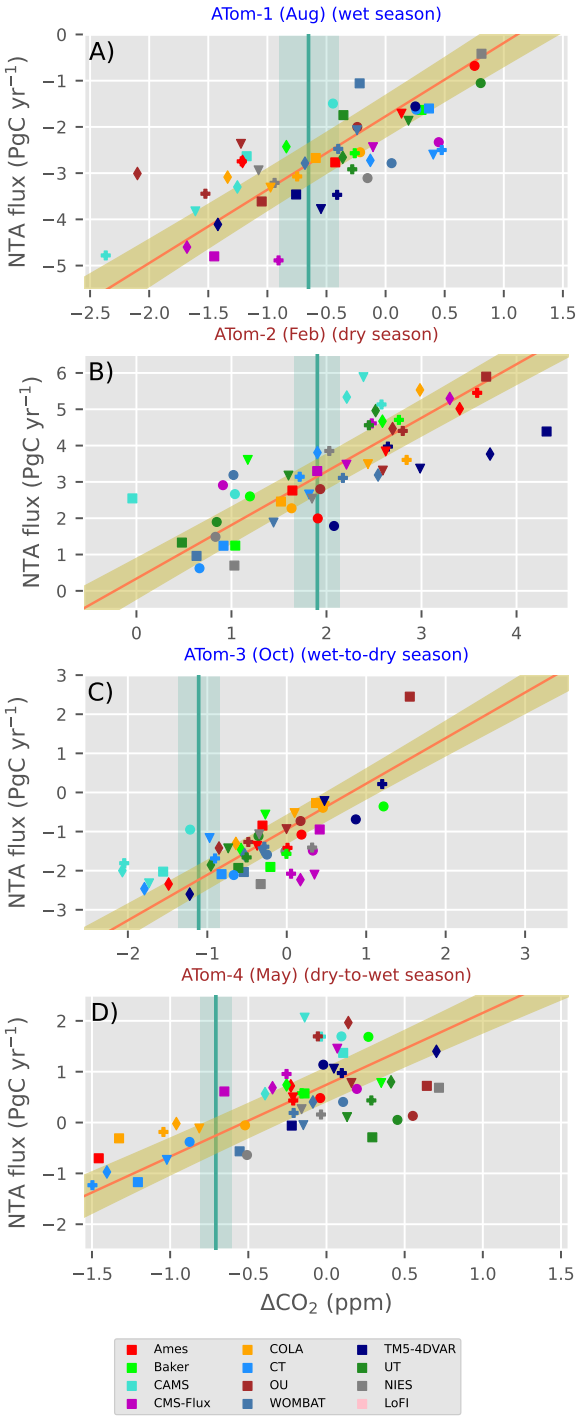

Figure S6. Same as Fig. 6 but with points colored by model. Point shape indicates experiment for IS (squares), OG (circles), LNLG (diamonds), and LNLGOGIS (triangles).

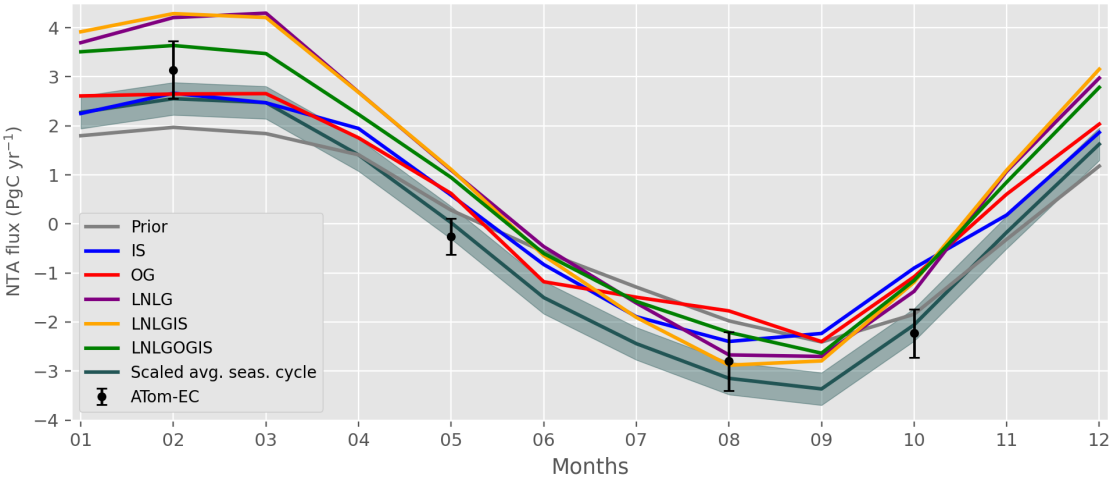

Figure S7. Average NTA land seasonal cycle (2016-2018). The ATom-EC and the scaled averaged seasonal cycle are also shown.

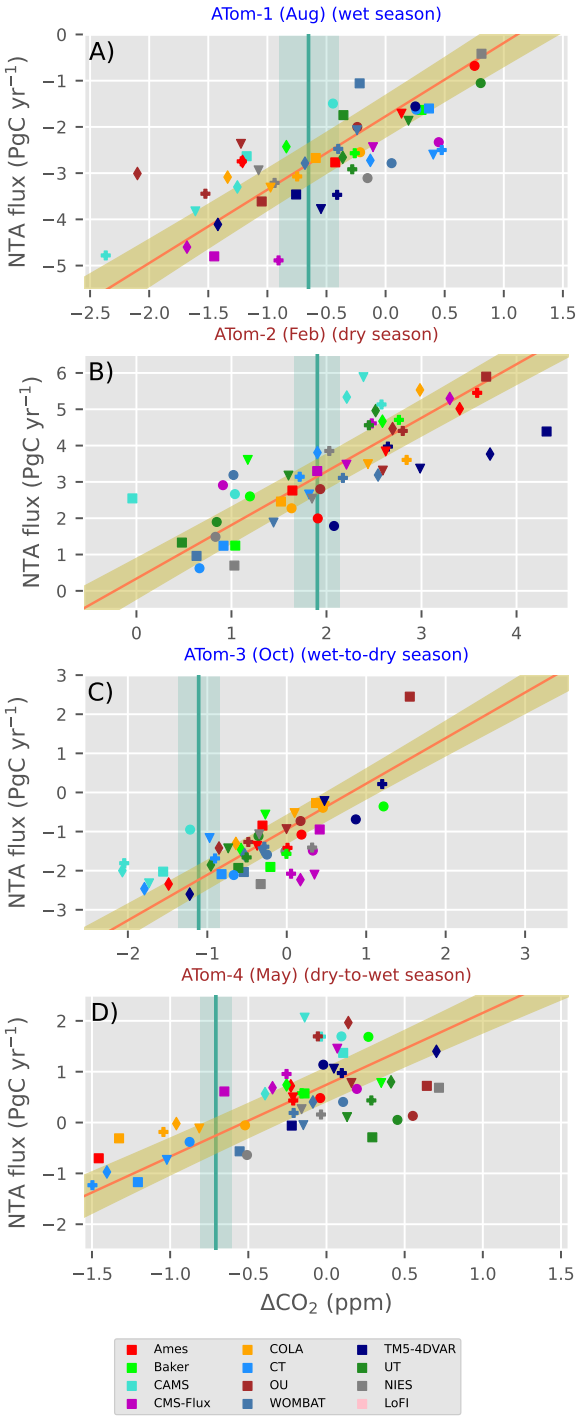

Figure S8. Same as Fig. 6 but with points colored by model. The 3 TM5 models are TM5-4DVAR, OU and CT, and the 5 GEOS-Chem models are Ames, CMS-Flux, COLA, UT and WOMBAT. Point shape indicates experiment for IS (squares), OG (circles), LNLG (diamonds), and LNLGOGIS (triangles).

References

Bowman, K. W., Liu, J., Bloom, A. A., Parazoo, N. C., Lee, M., Jiang, Z., ... Wunch, D. (2017, October). Global and brazilian carbon response to el niño modoki 2011-2010. *Earth and Space Science*, *4*(10), 637-660. doi: 10.1002/2016EA000204

Curtis, P. G., Slay, C. M., Harris, N. L., Tyukavina, A., & Hansen, M. C. (2018, September). Classifying drivers of global forest loss. *Science*, *361*(6407), 1108–1111. doi: 10.1126/science.aau3445

Hickman, J. E., Andela, N., Dammers, E., Clarisse, L., Coheur, P.-F., Damme, M. V., ... Bauer, S. E. (2021, November). Changes in biomass burning, wetland extent, or agriculture drive atmospheric nh $_3$ trends in select african regions. *Atmospheric Chemistry and Physics*, *21*(21), 16277–16291. doi: 10.5194/acp-21-16277-2021

Kiel, M., O'Dell, C. W., Fisher, B., Eldering, A., Nassar, R., MacDonald, C. G., & Wennberg, P. O. (2019, April). How bias correction goes wrong: measurement of affected by erroneous surface pressure estimates. *Atmospheric Measurement Techniques*, *12*(4), 2241–2259. doi: 10.5194/amt-12-2241-2019

Miyazaki, K., Bowman, K. W., Yumimoto, K., Walker, T., & Sudo, K. (2020, January). Evaluation of a multi-model, multi-constituent assimilation framework for tropospheric chemical reanalysis. *Atmospheric Chemistry and Physics*, *20*(2), 931–967. doi: 10.5194/acp-20-931-2020

O'Dell, C. W., Connor, B., Bösch, H., O'Brien, D., Frankenberg, C., Castano, R., ... Wunch, D. (2012, January). The ACOS co_2 retrieval algorithm – part 1: Description and validation against synthetic observationsthe ACOS co_2 retrieval algorithm – part 1: Description and validation against synthetic observations. *Atmospheric Measurement Techniques*, *5*(1), 99–121. doi: 10.5194/amt-5-99-2012

Ramo, R., Roteta, E., Bistinas, I., van Wees, D., Bastarrika, A., Chuvieco, E., & van der

Werf, G. R. (2021, February). African burned area and fire carbon emissions are strongly impacted by small fires undetected by coarse resolution satellite data. *Proceedings of the National Academy of Sciences*, *118*(9), e2011160118. doi: 10.1073/pnas.2011160118

van der Werf, G. R., Randerson, J. T., Giglio, L., van Leeuwen, T. T., Chen, Y., Rogers, B. M., ... Kasibhatla, P. S. (2017, September). Global fire emissions estimates during 1997–2016. *Earth System Science Data*, *9*(2), 697–720. doi: 10.5194/essd-9-697-2017

van Wees, D., & van der Werf, G. R. (2019, November). Modelling biomass burning emissions and the effect of spatial resolution: a case study for africa based on the global fire emissions database (GFED). *Geoscientific Model Development*, *12*(11), 4681–4703. doi: 10.5194/gmd-12-4681-2019

Yevich, R., & Logan, J. A. (2003, October). An assessment of biofuel use and burning of agricultural waste in the developing world. *Global Biogeochemical Cycles*, *17*(4), n/a–n/a. doi: 10.1029/2002gb001952